

# Mineral-guided molecular enrichment: An interfacial driving force for protocell emergence

Weifeng Chen, Rongfeng Zheng, Zhaosen Luo, Guoquan Wu, Jiayu Lei, Haochun Gou, Hao Li,

Zhili Wang & Guozhi Yu✉

## Abstract

A key challenge in the origin of life is forming molecularly crowded, compartmentalized systems from a dilute prebiotic environment. Here we show that mineral interfaces resolve this challenge by orchestrating the hierarchical assembly of nucleotides, proteins, and lipids. Specifically, we use silica as geochemically relevant scaffolds to drive spatially co-adsorption and enrichment of these biomacromolecules. These surfaces create concentration gradients that drive proto-metabolic flux, with assembled enzyme cascades mimicking the substrate channeling found in modern cells. Subsequently, lipids assemble around protein-coated mineral particles, templating membrane encapsulation that achieve selective compartmentalization of distinct catalytic cores, while maintaining permeability essential for small-molecule exchange and metabolic continuity. This synergistic mineral-guided process—integrating molecular crowding, interfacial catalysis, and the templated assembly of membranes—delineates a robust and multi-step pathway for protocell emergence. Our findings establish mineral surfaces as dynamic platforms for prebiotic systems chemistry, providing a unified mechanism that couples metabolism to compartmentalization under conditions relevant to the early Earth.

## Introduction

How the first living cells emerged from an abiotic planet remains one of the most fundamental questions in science. A central requirement for life's origin is the formation of molecularly crowded, compartmentalized systems capable of sustaining metabolic cycles and preserving informational polymers<sup>1,2,3</sup>. The primordial Earth, however, likely presented a vast and dilute aqueous environment, posing a fundamental thermodynamic paradox: the very medium that facilitates prebiotic chemistry also hinders the spontaneous assembly and interaction of macromolecules. Overcoming this dilution to achieve the localized, high-concentration conditions necessary for biochemical complexity is therefore a critical hurdle in any plausible origin-of-life scenario<sup>4,5</sup>.

Mineral-water interfaces have long been implicated as crucial loci for prebiotic chemistry, offering a potential solution to the dilution problem. Geochemically abundant surfaces, from clays to silica, are known to selectively adsorb and concentrate organic molecules, catalyze the formation of biopolymers such as peptides and nucleic acids<sup>6, 7, 8, 9, 10</sup>, and generate electrochemical gradients that could power primitive metabolism<sup>11, 12</sup>. Furthermore, studies

have shown that charged mineral interfaces can mediate the phase separation of polymers into distinct compartments<sup>13</sup>, and that wet-dry cycles at these interfaces can drive non-equilibrium processes<sup>14</sup>. While these individual functions highlight the potential of minerals as geochemical scaffolds, however, a unified framework that integrates molecular enrichment, proto-metabolism, and compartmentalization into a single, continuous pathway has remained elusive<sup>15, 16</sup>. Here we show that mineral interfaces act as dynamic platforms that orchestrate the hierarchical assembly of protocellular structures, directly driving their emergence. We propose a mechanism of mineral-guided surface molecular enrichment (MSE), where geochemically relevant mineral surfaces first mediate the co-adsorption and spatial organization of key biomacromolecules. This process creates a crowded two-dimensional reaction space, establishing the conditions necessary for the emergence of surface-bound, proto-metabolic pathways. Subsequently, these functionalized protein-mineral complexes serve as templates for the assembly of lipid membranes, leading to the formation of discrete, catalytically active compartments.

Our findings reveal that mineral surfaces not only concentrate diverse biomolecules but also support the spatial organization of multi-enzyme cascades, creating a configuration that facilitates coupled catalytic reactions in a process analogous to substrate channeling in biological cells. This synergistic pathway, which integrates molecular crowding, interfacial catalysis, and membrane formation, delineates a robust and plausible route from disorganized molecules in a prebiotic soup to functionally integrated, protocellular systems. Our work thus establishes mineral surfaces as foundational and active platforms for prebiotic systems chemistry, offering a coherent mechanism that couples interfacial metabolic activity with hierarchical self-assembly under conditions relevant to the early Earth.

## Results

**Mineral-mediated stable co-enrichment of different types of biomolecules** To probe how geochemical interfaces could have organized prebiotic matter, we examined the ability of mineral particles to concentrate and co-localize DNA, RNA and protein. Considering reports indicating that relatively unstructured protein segments are preferentially adsorbed by silica<sup>17, 18, 19</sup>, and that primordial amino-acid condensation likely produced intrinsically disordered sequences, we performed all experiments using two fusion constructs that meet these criteria: FUS-IDR-sfGFP<sup>20</sup> and BFP-hnRNPA1-IDR<sup>21</sup> (sequences detailed in Supplementary Table 1). Silica microspheres adsorbed Cy3-DNA, FITC-RNA and BFP-tagged protein, each detected in its respective fluorescence channel (Fig. 1a–c), and—crucially—supported the simultaneous co-adsorption of all three biomolecular classes at their surfaces. Quantitative fluorescence mapping and line-scan analysis revealed tight spatial overlap of the three signals at the silica interface (Fig. 1d–e; Supplementary Fig. 3), consistent with the formation of locally enriched microenvironments that could concentrate reaction substrates and intermediates to promote surface-confined reaction fluxes akin to protometabolic cycles. We also observed protein-coated particles sequestered within small gas bubbles (Supplementary Fig. 2), these gas bubbles may have served as early barriers, maintaining molecular organization in a way that could have supported proto-metabolic processes, without implying the formation of fully encapsulated, membrane-like compartments. Finally, the adsorbed material proved resilient to simulated environmental flux: after repeated wash cycles (10×), individual FUS-IDR-GFP

molecules and ternary protein–RNA–DNA assemblies remained detectable on  $\text{CaCO}_3$ , montmorillonite and  $\text{SiO}_2$  (Fig. 1f–g). Crucially, this co-adsorption is highly stable against physical perturbation (Fig. 1f,g), demonstrating that these enriched microenvironments could persist within the dynamic conditions of the early Earth. Together, these observations identify diverse mineral surfaces as robust scaffolds for resisting dilution and for creating spatially distinct, semi-stable niches that could scaffold early, surface-mediated proto-metabolic and compartmentalization processes. Extending this, we found that elevated temperature (70 °C), plausible for early Earth, further enhanced protein adsorption across all tested minerals (Supplementary Fig. 1), with montmorillonite showing the highest capacity owing to its layered, negatively charged architecture, suggesting that minerals could have simultaneously concentrated and stabilized primordial biomolecules under geologically relevant conditions.

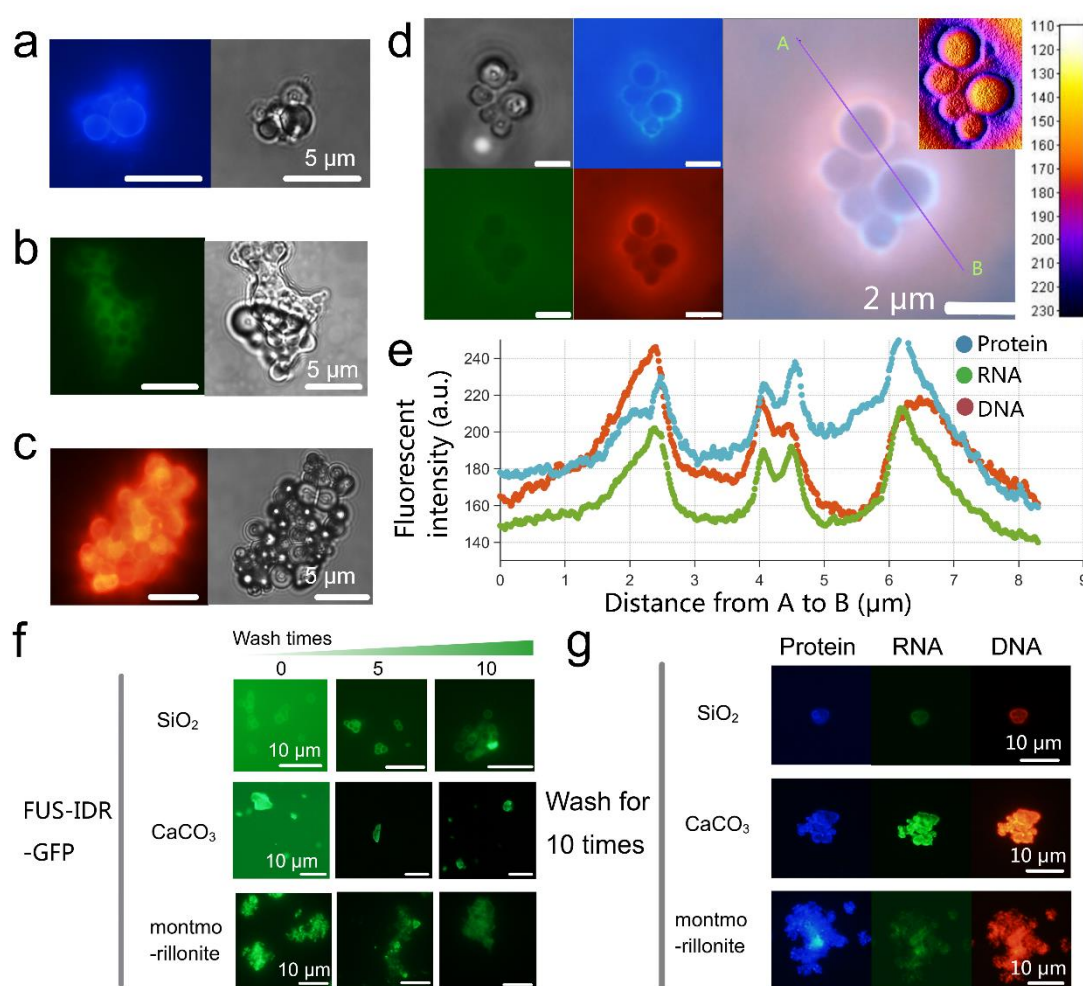


**Figure 1 | Co-adsorption, spatial co-localization, and retention stability of biomacromolecules mediated by minerals.** a-c, Single-channel fluorescence images of individually labeled biomolecules adsorbed on silica particles: (a) BFP-hnRNPA1-IDR protein (blue), (b) FITC-labeled RNA (green), and (c) Cy3-labeled DNA (red). The background shows corresponding bright-field images. Scale bars, 5  $\mu\text{m}$ . d, Composite analysis images of co-adsorbed biomolecules: from left to right, bright-field, individual fluorescence channels (protein in blue; RNA in green; DNA in red), merged fluorescence image, and an

RGB integrated fluorescence heatmap inset (color bar represents cumulative intensity, a.u.). Scale bar, 2  $\mu\text{m}$ . e, Fluorescence intensity profiles along the path A-B in d (protein in blue; RNA in green; DNA in red), showing the spatial co-localization of the three biomacromolecules. f, Retention of FUS-IDR-GFP fluorescence (green) on  $\text{SiO}_2$ , montmorillonite, and  $\text{CaCO}_3$  mineral surfaces after 0, 5, and 10 wash cycles. Each row of images was taken with the same acquisition parameters. Scale bar, 10  $\mu\text{m}$ . g, Co-adsorption and retention of proteins (blue), RNA (green), and DNA (red) on specified mineral surfaces after 10 wash cycles. Scale bar, 10  $\mu\text{m}$ .

**Heterogeneous molecular layering and limited fluidity on mineral surfaces** After analyzing the adsorption of three types of biomacromolecules onto different mineral particles, we proceeded to investigate the adsorption of proteins onto silica particles as a case study to further delineate the physical characteristics of MSE. We start with a quantitative investigation of the protein shell distribution on the surfaces of spherical silica particles. Figure 2.a depicts the coordinate system alongside additional parameters (see to Supplementary Note 1 for mathematical details). Figure 2b illustrated that the radial fluorescence intensity profile was deconvoluted with a dual-exponential decay model to quantify the spatially structured molecular layers, expressed as  $I(r) = \alpha \cdot \exp(-\lambda_1 r) + \beta \cdot \exp(-\lambda_2 r) + bg$ . This model delineates two distinct physical regimes: (i) a near-field component characterized by amplitude  $\alpha$  and decay rate  $\lambda_1$ , representing a dense layer of FUS-IDR-GFP firmly adhered to the mineral surface; and (ii) a far-field component defined by amplitude  $\beta$  and decay rate  $\lambda_2$ , corresponding to a more diffuse corona of weakly interacting molecules in equilibrium with the bulk solution. We examined the parameter space across different macromolecular concentrations to comprehend the distribution of various parameters (Fig. 2c). The radar plot results demonstrate that, throughout both high- and low-concentration regimes,  $\alpha$ ,  $\beta$ ,  $\lambda_1$ , and  $\lambda_2$  exhibit extensive variability, but the background ( $bg$ ) stays distinctly separate (the average  $bg$  for high and low concentration groups are 55.04 and 21.08, a.u., respectively). This seemingly unreasonable parameter distribution indicates a credible scenario: significant particle heterogeneity throughout the MSE system. This variety likely results from differences in inorganic particle geometry and surface characteristics, random fluctuations in local bulk concentrations, and interactions among adjacent particles, therefore providing biomacromolecules with a wide range of ecological niches.

To elucidate the origin of surface permeability of the interfacial protein corona, we employed fluorescence recovery after photobleaching (FRAP) to evaluate the fluidity of the FUS-IDR-GFP corona. Post-photobleaching, the fluorescence of surface shells was seen to recover 20% of its initial intensity over 300 seconds—a slight yet noteworthy fluidity (Fig. 2d-e). To address potential hydrodynamic flushing in early-Earth environments, we introduced buffer rinsed GFP[ $\text{SiO}_2$ ] and BFP[ $\text{SiO}_2$ ] and measured their fusion rates. Contact fusion studies with GFP/BFP-coated silica particles demonstrated prolonged intermixing between neighboring compartments for 12 hours (Fig. 2f). While the overall degree of molecular intermixing, as measured by Mander's coefficients ( $M_6$ ,  $M_3$ ), did not show a statistically significant change over 12 hours ( $p > 0.05$ , Fig. 2g), we observed a slow redistribution of fluorescent proteins between adjacent particles. This indicates that the protein corona, while largely stable, possesses a limited fluidity. This combination of long-term stability and slow short-range dynamics is functionally critical: it allows for the preservation of distinct molecular identities

in neighboring compartments, a prerequisite for functional specialization, while still permitting the interfacial molecular movement necessary for proto-metabolic processes. This dynamic activity validates the mineral interface's ability to facilitate substrate movement crucial for protometabolic continuity. Simultaneously, the slow yet persistent macromolecular migration preserves heterogeneity within the inorganic-particle surface layer, establishing a foundation for functionally separate metabolic compartments analogous to modern subcellular structures—or even tissues.

Prompted by fluidity and fusion dynamics, we investigated whether MSE could complement liquid-liquid phase separation (LLPS) in dilute prebiotic environments. Fluorescence intensity comparisons revealed LLPS condensates exhibited significantly higher biomolecular sequestration than MSE (Fig. 2h-i). MSE's comparatively diffuse enrichment profile (Fig. 2i) confirms its intrinsically weaker sequestration efficiency—a direct consequence of its reliance on surface adsorption rather than bulk demixing. Paradoxically, this apparent “limitation” resolves a prebiotic paradox: in primordial settings where biomolecule concentrations were too low for spontaneous LLPS nucleation<sup>22</sup>, MSE provided a critical pre-concentrating step. Consistent with this view, our theoretical map (Fig. 2j) resolves the interfacial gradient  $\chi(r, D)$  over diffusion coefficients and distance from the surface:  $\chi(r, D) = c_{surf} - c_{bulk}$  and decays exponentially with  $r$ , with a penetration length that increases with  $D$  ( $\lambda \propto D^{-1/2}$ ), such that higher diffusivity maintains elevated  $\chi$  over longer ranges while lower  $D$  confines enrichment to a thin interfacial layer. Under the parameters used here ( $c_{surf} = 3\mu M$ ;  $c_{bulk} = 1\mu M$ ;  $c_{crit} = 4\mu M$ ), the  $\chi$ —surface remains below the LLPS threshold plane across the explored domain, indicating that MSE alone does not trigger LLPS in this regime but shifts the system closer to the critical manifold. In line with the theoretical framework, modest parameter changes (mimicking the fluctuations of plausible cases) —such as increasing  $c_{surf}$  or  $D$ , decreasing  $k_{off}$  or effectively lowering the threshold ( $c_{crit}$ ) or increasing surface capacity ( $c_{max}$ ) —would be expected to move the interfacial region into the nucleation-permissive regime near the mineral surface (Supplementary Fig. 3).

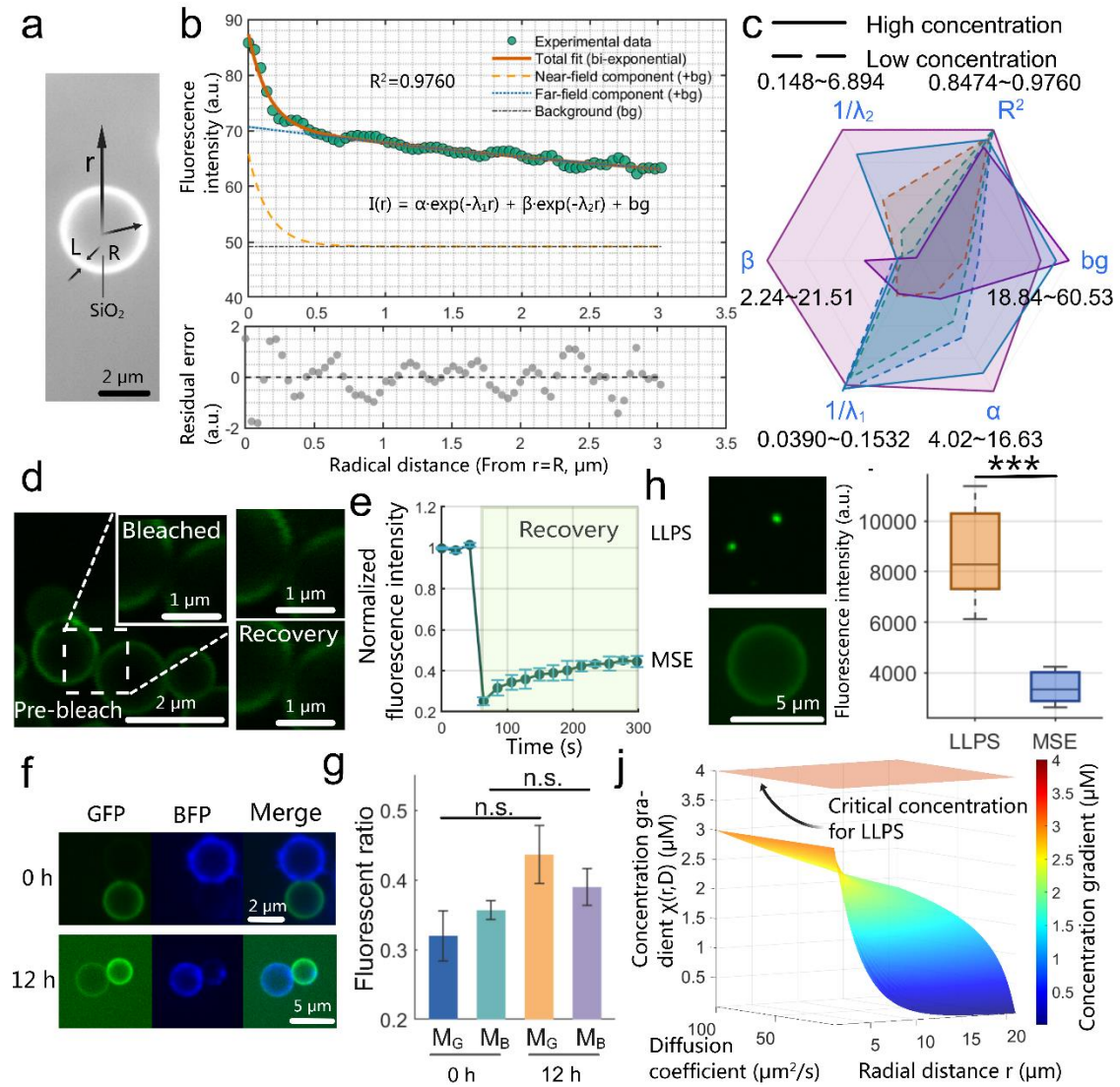


**Figure 2 | Characterization of the physical properties of molecular enrichment on mineral surfaces.**

a, Schematic representation of the radial coordinate system for a spherical silica particle with radius  $R$ . The shell thickness ( $L$ ) and distance from the surface ( $r$ ) define the spatial parameters of protein dispersion.

b, The radial fluorescence intensity distribution was fitted using a double exponential decay model:  $I(r) = \alpha \exp(-\lambda_1 r) + \beta \exp(-\lambda_2 r) + bg$ . The top panel shows experimental data points and the model fit curve ( $R^2 = 0.9760$ ), and the bottom panel shows a residual plot indicating a random error distribution.

c, Radar plot of model fitting parameters at different protein concentrations. Three representative samples were chosen for each concentration group.

d-e, Time-lapse images (d) and quantitative analysis (e) of fluorescence recovery after photobleaching (FRAP) of a FUS-IDR-GFP protein corona on a silica particle surface, showing an approximately 20% recovery in fluorescence intensity over 300 seconds. Error bars represent the standard deviation of three repeated experiments.

f, Fusion kinetics of pre-washed FUS-IDR-GFP /BFP-hnRNP1-IDR labeled protein-silica particles over 12 hours. Scale bar, 5  $\mu\text{m}$ .

g, Mander's coefficient ( $M_B/M_G$ ) quantitatively analyzes the degree of molecular intermixing during fusion. Data are presented as mean  $\pm$  standard deviation ( $n = 3$  pairs of particles per group).

h-i, Fluorescence images (h) and quantitative analysis of fluorescence intensity (i) of liquid-liquid phase separation (LLPS) condensates (top) and MSE droplets (bottom) under identical conditions, confirming that LLPS has a higher molecular enrichment efficiency ( $**p < 0.001$ ; unpaired two-tailed  $t$ -test;  $n = 20$  per group).

j, 3D simulation of a

concentration gradient formed by diffusion (along the radial axis  $r$ ).

**Silica-scaffold-supported metabolic activity** Building upon the observed fluidity of the interfacial protein corona, we next investigated whether these dynamic mineral scaffolds could organize and support functional, multi-step biochemical reactions, a prerequisite for proto-metabolism. To probe this, we assembled a two-step enzyme cascade on silica microspheres. The system comprised glucose oxidase (GOx) and horseradish peroxidase (HRP), which act sequentially to convert glucose into  $H_2O_2$  and then utilize the  $H_2O_2$  to oxidize Amplex Red into the fluorescent product, resorufin<sup>23 24</sup>. This spatial juxtaposition is known to enhance overall reaction efficiency by minimizing the diffusion of intermediates, a process analogous to substrate channeling in contemporary cells<sup>25</sup>. We co-localized GOx and HRP onto the silica surfaces along with two distinct IDR-fused fluorescent proteins (FUS-IDR-GFP and hnRNPA1-IDR-BFP), which served to delineate the reactive surface and promote enzyme retention. After removing unbound enzymes via washing, fluorescence microscopy confirmed the stable co-localization of the fluorescent marker proteins on the particle surfaces. Crucially, the robust emission from resorufin, localized exclusively at the mineral interface, provided direct evidence of coupled catalytic activity. These findings establish that mineral interfaces can serve as effective scaffolds for assembling synergistic, proto-metabolic networks, thereby creating a foundation for the subsequent evolution of compartmentalized protocellular systems.

Given that the primordial soup likely contained both nucleic acids and proteins, we further sought to determine if such mineral interfaces could also support enzymatic processes involving nucleic acids. We performed a reverse transcription-polymerase chain reaction (RT-PCR) assay directly within a suspension of silica particles, monitoring the amplification of a target RNA template via SYBR Green I fluorescence. Time-lapse microscopy and quantitative fluorescence analysis revealed a progressive, cycle-dependent intensification of the SYBR Green I signal localized on the silica surfaces. This demonstrates that the enzymatic machinery for both reverse transcription and DNA amplification remains functional when adsorbed onto the mineral particles, suggesting these surfaces could have supported not only primordial metabolism but also rudimentary forms of information replication and transfer.



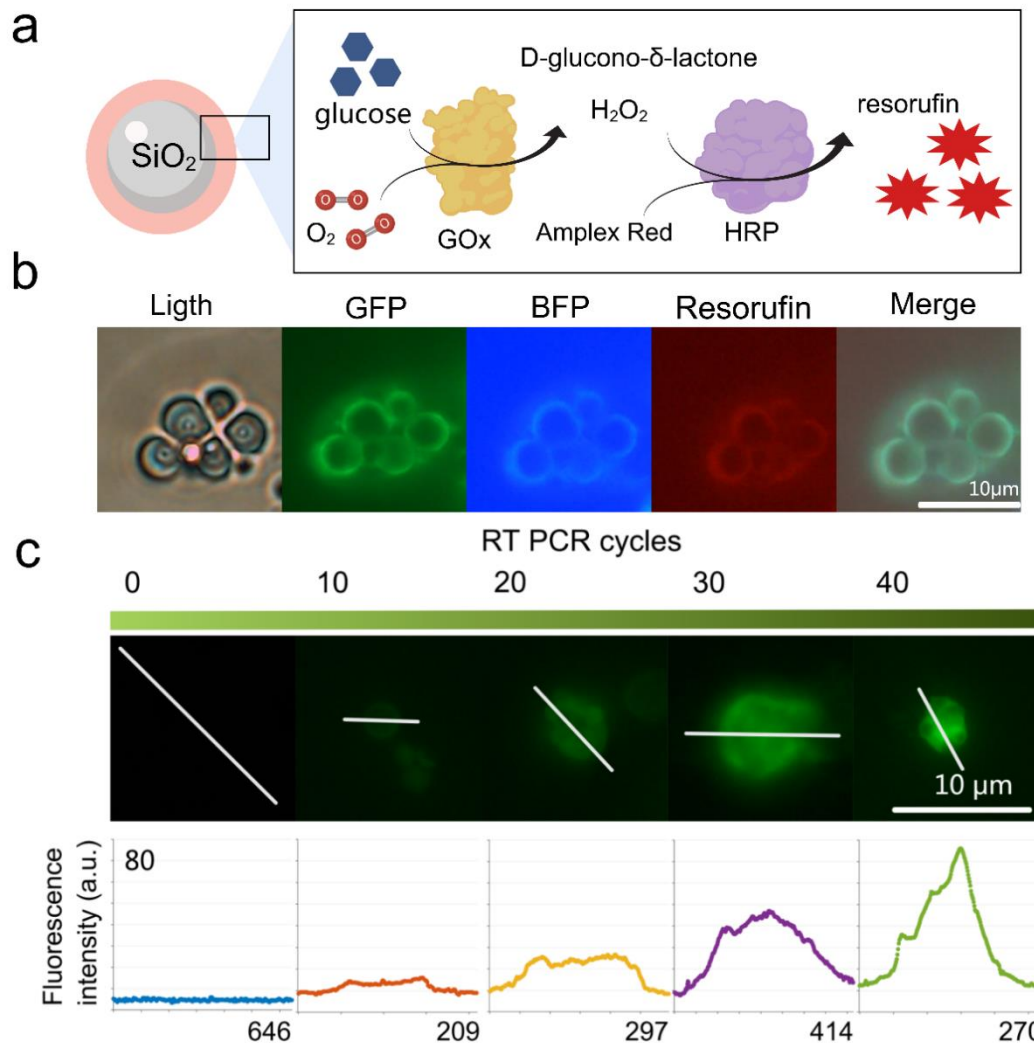


**Figure 3 | Enzyme cascade assembly and imaging on silica particles.** a, Schematic diagram of the glucose oxidase (GOx) and horseradish peroxidase (HRP) cascade reaction. GOx catalyzes the conversion of glucose to D-glucono- $\delta$ -lactone and hydrogen peroxide, and HRP subsequently uses the hydrogen peroxide to oxidize Amplex Red into the fluorescent product resorufin (red star). b, Microscopic images (from left to right): bright-field (light), FUS-IDR-GFP, BFP-hnRNPA1-IDR, resorufin fluorescence (red), and merged channel images. The images show that the FUS-IDR-GFP / BFP-hnRNPA1-IDR signal and resorufin synthesis co-localize on the silica surface, confirming the immobilization and functional coupling of the proteins. Scale bar, 10  $\mu$ m. c, Reverse transcription PCR in the presence of silica particles. The top image sequence shows the increasing intensity of SYBR Green I fluorescence with the number of cycles, all images acquired with the same parameters. The bottom graph shows a histogram of light intensity scans along the equal-length straight lines in the top images (The horizontal axis denotes the number of pixels).

**Mineral-templated formation of metabolically active protocell-like compartments** After confirming that mineral surfaces facilitate enzyme colocalization and functional coupling (Fig. 3c), we proceeded to investigate how these pre-organized molecular architectures could



template higher-order structural complexity—specifically, whether and how these protein-mineral composites might direct the formation of spatially confined lipid-protein assemblies capable of metabolic compartmentalization. In control systems (Fig. 4b), palmitoleic acid primarily generates free lipid droplets (arrowheads) with occasional adsorption onto bare silica surfaces (arrows), indicating fundamental interfacial activity. The introduction of FUS-IDR-GFP protein coronas (Fig. 4c, P/G/B[SiO<sub>2</sub>] denotes protein/GFP/BFP-coated silica particles) significantly alters lipid distribution. Pre-coated silica particles (Fig 4.c) serve as templates for hybrid assemblies in which lipids co-localize with protein coronas (arrows), but residual lipid droplets remain (arrowheads), establishing a dynamic balance between membrane-bound and mobile lipid phases. Three-dimensional reconstructions clarified the structural organization, illustrating lipid-protein co-localization (arrow) in conjunction with enduring free lipid droplets (arrowhead, Fig. 4d). Quantitative colocalization analysis demonstrated a considerable overlap between GFP and PAL signals (Fig. 4e-f). Because such lipid-protein coatings could plausibly modulate molecular exchange, we assessed the functional consequence on permeability: silica particles bearing Cy5-PAL(+) exhibited reduced uptake of the macromolecular probe FITC-streptavidin compared with lipid-free controls (–) (Fig. 4h). Quantitative analysis showed an approximately 12.5% decrease in normalized fluorescence intensity for the Cy5-PAL(+) group ( $p < 0.05$ ,  $n = 9$  per group) (Fig. 4i), consistent with a modest reduction in macromolecular permeability associated with the lipid-protein assemblies.

Upon the amalgamation of GFP- and BFP-coated assemblies for 2h (Fig 4.g), lipid membranes selectively encapsulated unique protein-mineral complexes, resulting in compartments that preserved discrete GFP or BFP identities. This segregation indicates that lipid layers function as barriers that inhibit the intermingling of surface-bound proteins. This striking result demonstrates that the mineral-protein cores act as templates, guiding lipid assembly to form distinct, non-mixing compartments. This process achieves selective encapsulation, creating a population of heterogeneous protocells from a common pool of molecules—a rudimentary form of cellular individuation. The compartments differed in dimensions, with lipid membranes assuming forms shaped by the underlying mineral substrate and protein layers. By expanding this approach, we illustrate that these hybrid assemblies facilitate enzyme-mediated proto-metabolic activity via spatially regulated reaction-diffusion dynamics (Fig. 4k). The incorporation of a GOx/HRP cascade, identical to that seen in Fig. 3, within the protein-lipid-mineral framework facilitated the monitoring of reaction partitioning. Fluorescence mapping demonstrated that resorufin synthesis was selectively localized at SiO<sub>2</sub> surfaces adorned with both enzymes (Fig. 4k). The tests depicted in Fig. 4k and Fig. 3f were performed using identical doses of enzymes and substrates. Despite the former demonstrating extended reaction and microscope exposure durations, its red fluorescence intensity was diminished, indicating that the lipid membrane possesses comparatively limited permeability to the substrates, particularly glucose.

And interestingly, the ratio-dependent shift from mineral-anchored composite coronas (high GFP/Cy5-PAL) to free lipid condensates (low ratio) mirrors a conceivable prebiotic process in which protocell membranes transitioned from mineral-scaffolded assemblies to autonomous condensates (Fig. 4j). At a low lipid-to-protein ratio, the two components spread over the silica surface to generate a quasi-uniform shell (arrow), whereas at a high ratio they co-

localize exclusively outside the particles, producing a dense, solid condensates (arrow head). The conflict at the interface between surface-adhesive molecules and lipid self-assembly forces reflects the proposed emergence of primitive cellularity, indicating that analogous physicochemical gradients on early Earth may have facilitated the development of stable, self-sustaining protocells.

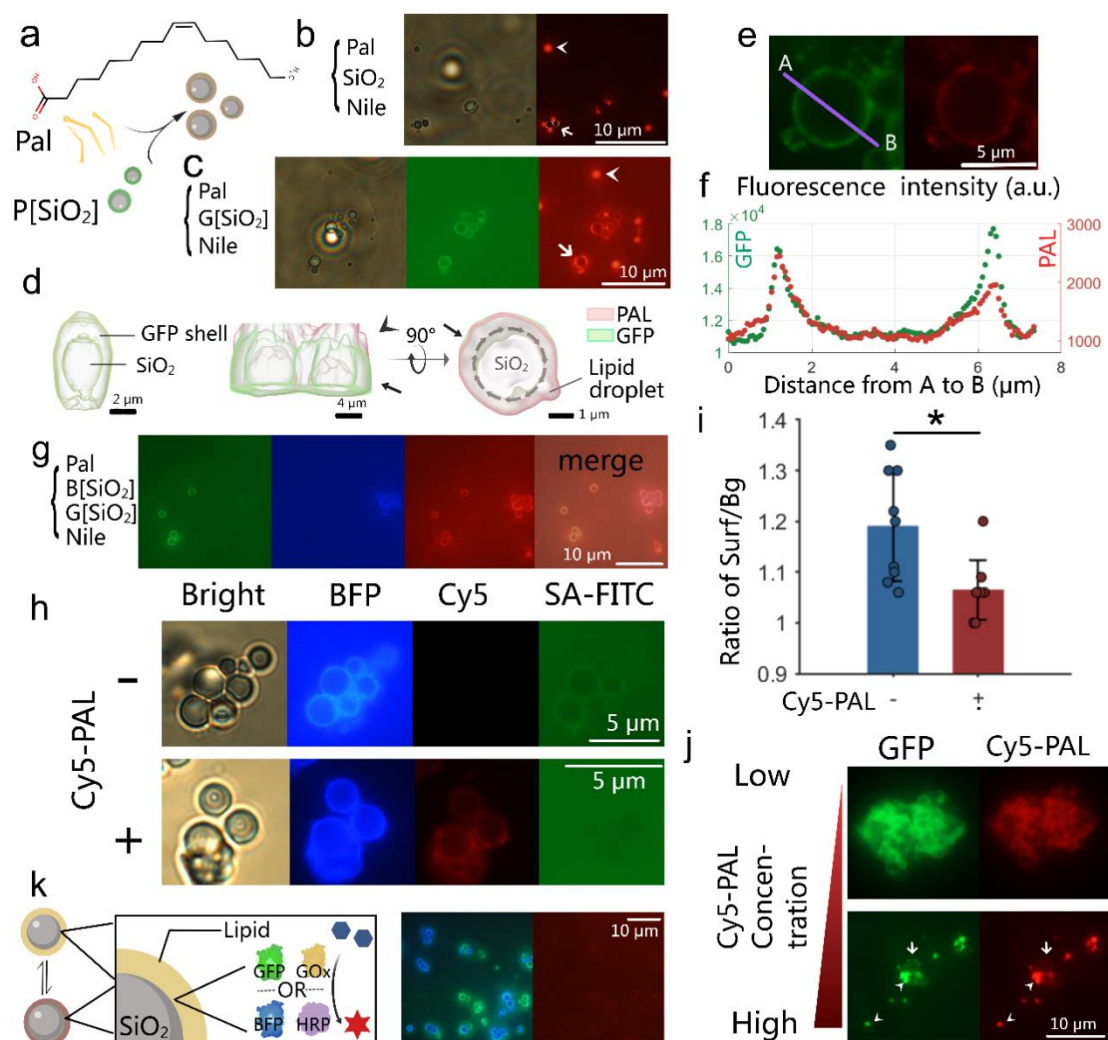


**Figure 4 | Hierarchical assembly of protocell-like compartments through silica-protein-lipid synergy.** a, Schematic diagram of the experimental process related to b and c, where the chemical formula represents the palmitoleic acid (PAL) used in the experiment. b, Control system (silica + lipid). The left image is a bright-field image of a silica particle with a small amount of adsorbed lipid droplets. The right image is the corresponding Nile Red fluorescence (red) image, highlighting both free lipid droplets (arrow) and adsorbed lipid droplets (arrowhead). c, Protein-guided lipid assembly (silica + GFP + PAL). From left to right: bright-field image; GFP fluorescence (green) confirming the formation of a uniform protein corona; Nile Red channel (red) showing co-localization of the lipid membrane with the protein-coated particle (arrowhead), with some free droplets still present (arrow). d, 3D reconstructed image from optical sections, showing lipid-protein co-localization (arrowhead) and free lipid droplets (arrow). e-f, Co-localization analysis of GFP and PAL on the same silica particle surface. f is the quantitative intensity profile along segment AB in e. g, Compartmentalized hybrid system with mixed

GFP+BFP assemblies. From left to right: GFP (green) and BFP (blue) labeled compartments remain separate; merged image confirms that a continuous lipid envelope encapsulates distinct protein-mineral cores. h, Permeability assay using FITC-streptavidin on silica-BFP particles with (+) or without (-) attached Cy5-PAL. i, Quantitative analysis of the results in h ( $n = 9$  per group,  $p < 0.05$ ). j, Interaction of GFP and Cy5-PAL with silica particles at different molar ratios. At low ratios, the two components spread on the silica surface to form a quasi-uniform shell (arrowhead); at high ratios, they co-localize outside the particle to form a dense, solid-state condensate (arrow). k, Metabolic coupling on lipid-encapsulated  $\text{SiO}_2$  particles. The left diagram is a schematic of the enzyme-coupled hybrid assembly, and the right image shows that resorufin fluorescence (red) synthesis is selectively localized on the  $\text{SiO}_2$  surface with both enzymes.

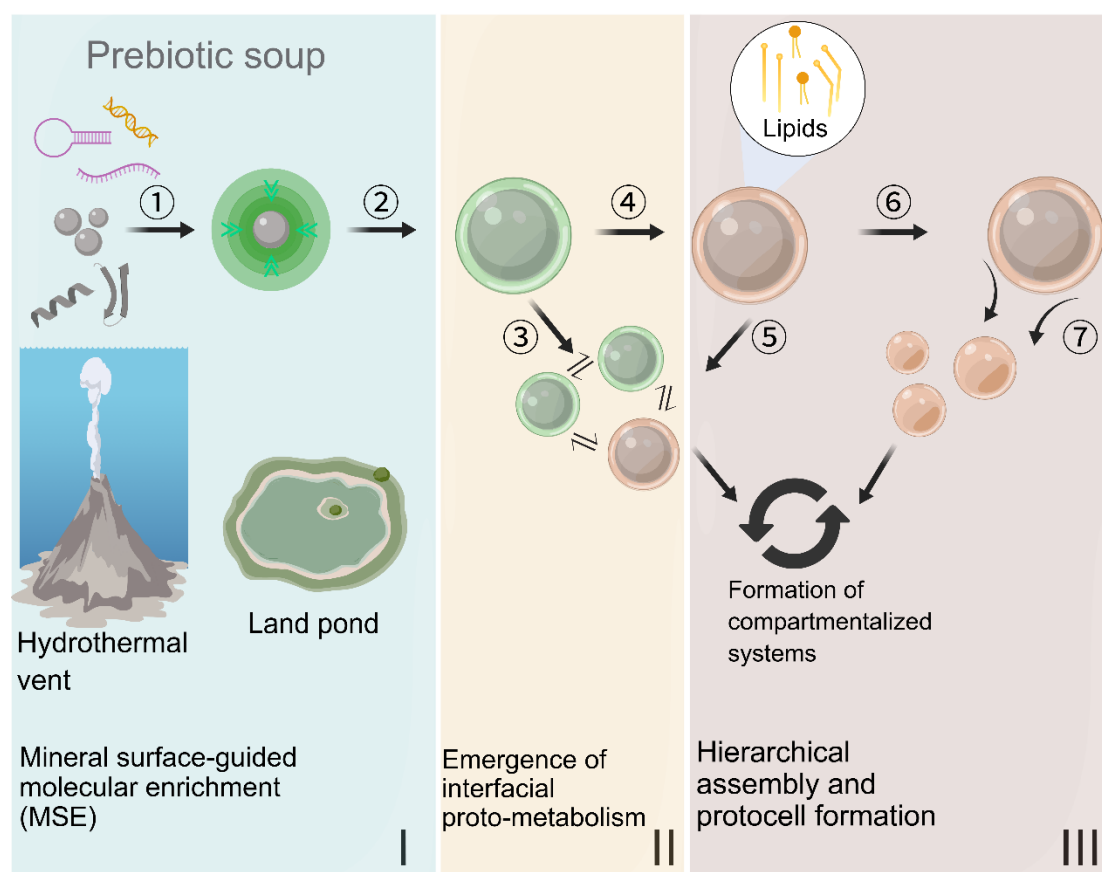


**Figure 5 | An integrated model for mineral-guided protocell emergence.**

(I) Mineral surface-guided molecular enrichment (MSE). In prebiotic environments such as hydrothermal vents or land ponds, essential biomolecules including nucleic acids and peptides co-adsorb onto mineral surfaces (1), concentrating them and overcoming the dilution problem inherent to the prebiotic soup.

(II) Emergence of interfacial proto-metabolism. The resulting molecularly crowded interface facilitates enzyme cascades (2), establishing a proto-metabolic system analogous to substrate channeling. This system maintains dynamic exchange with other functionalized particles (3) or with ensuing lipid-coated assemblies (4).

(III) Hierarchical assembly and protocell formation. Lipids subsequently assemble around the protein-mineral composites, templating the formation of a membrane boundary (5). This process enables the selective encapsulation of distinct catalytic cores (6), giving rise to compartmentalized systems that maintain functional heterogeneity and metabolic continuity, ultimately leading to the formation of a

protocell (7).

## Discussion

Our results delineate a mineral-guided strategy for protocell emergence that directly tackles the persistent issues of molecular dilution and uncontrolled compartmentalization. Prior studies emphasized the efficiency of bulk liquid–liquid phase separation (LLPS) as a mechanism for biomolecular condensation<sup>26</sup>. However, such processes typically require micromolar to millimolar concentrations seldom attainable in prebiotic settings. By contrast, we show that mineral-surface enrichment (MSE) generates interfacial microenvironments that locally lower the threshold for phase transitions. This divergence from bulk LLPS highlights how dimensional reduction at mineral interfaces creates a distinct physicochemical regime—less efficient in sequestration, yet particularly adapted to dilute primordial conditions.

Mineral-mediated organization has long been implicated in origins-of-life chemistry. Clay and silica surfaces are known to adsorb and even catalyze the polymerization of nucleotides and peptides<sup>10, 27</sup>, while recent biophysical studies demonstrate that charged or wet-dry cycled interfaces can promote molecular crowding and phase transitions<sup>28</sup>. Our observation that MSE co-localizes nucleic acids, proteins, and lipids under dilute conditions aligns with prior observations and offers experimental evidence that mineral surfaces function as dynamic controllers of molecular assembly rather than merely passive scaffolds. Furthermore, silica-bound protein coronas reduce the entropic cost of lipid ordering, consistent with models suggesting that pre-existing scaffolds promote amphiphile self-assembly<sup>29</sup>, analogous to cytoskeletal templating in modern cells.

Our findings surpass previous models by including conflicting protocell scenarios into a continuous, mineral-directed pathway. Hybrid protocell systems have demonstrated that coacervates can be cloaked by fatty acid layers, yielding semi-permeable vesicles with selective uptake. We show that a similar transition can occur at mineral interfaces, where lipid encapsulation of protein–mineral composites yields distinct, metabolically active compartments. This process connects surface-anchored complexes to autonomous vesicles, so reconciling the seeming opposition between the "membrane-first"<sup>30</sup> and "metabolism-first"<sup>31</sup> models. Moreover, by sustaining enzyme cascades reminiscent of substrate channeling and supporting nucleic acid replication on surfaces, MSE offers a framework that couples enrichment, metabolism, and compartmentalization within geochemically plausible contexts. Taken together, our work demonstrates that mineral interfaces act as active organizers of protocell emergence—contrasting with bulk-phase models, supporting prior observations of interfacial chemistry, and extending the field by unifying disparate scenarios into a coherent pathway. This mineral-mediated hierarchy provides a versatile platform for systems chemistry on the early Earth and suggests testable routes for reconstructing the origins of cellular complexity.

## Methods

**Extraction and Preparation of Fluorescent Proteins** The plasmids of the two fluorescent proteins (for the sake of simplicity, all GFP in this article represents FUS-IDR-GFP, and all BFP represents EBFP-hnRNPA1-IDR) were separately transformed into the *E. coli* BL21(DE3) strain. The transformed bacteria were cultured in LB medium containing kanamycin at 37 °C. When

the optical density (OD) value reached 0.4-0.6, isopropyl  $\beta$ -D-1-thiogalactopyranoside (IPTG) (with a final concentration of 0.3 mM, Beyotime) was added, and the bacteria were then incubated with shaking at 28 °C for 8h. Recombinant bacterial cells expressing fused-proteins were pelleted by centrifugation (5,000×g, 10 min, 18°C). Pellets were resuspended in non-denaturing lysis buffer (pH=8.0) and disrupted via sonication (10 s on/off cycles, 300W, 20min). Clarified lysates (centrifuged for 30min at 4°C, 12000g) were loaded onto nickel-chelated agarose columns (Beyotime) pre-equilibrated with non-denaturing lysis buffer (pH=8.0), followed by 0.5 h incubation at 4°C for protein binding. The column underwent sequential washing (5-column volumes, non-denaturing washing buffer (pH=8.0) and elution (non-denaturing elution buffer (pH=8.0)). To recover target proteins, purified proteins were dialyzed overnight at 4°C against storage buffer to exchange buffer components. The concentration of proteins was determined using a BCA kit (Beyotime). See protein sequences for table S1. And the formulations of various buffer solutions are shown in Table 2-5.

**Adsorption of Different Bio-Macromolecules on the Surfaces of Various Minerals** In both Figure 1 and Figure S1, all minerals, DNA, and RNA were dissolved in a 50 mM tris-HCL (pH 7.4) buffer solution, while proteins were dissolved in a buffer solution containing 50 mM Tris-HCl and 125 mM NaCl (pH 7.4). In the corresponding experiments, the final concentration of proteins (the sequence information is shown in Supplementary Table 1) was 0.5  $\mu\text{g}/\mu\text{l}$ . The final concentration of DNA (18S rRNA Cy3 probe, Beyotime) and RNA (random sequence, 5'-FITC labeled CAACGACUCGCGCUUAAUUA, synthesized by Sangon Biotech) was 25  $\mu\text{g}/\text{ml}$ . The final concentration of various minerals was 2.5 mg/ml. Unless otherwise specified, all microscopic photographs were taken using an Olympus BX53 microscope.

**Contact silica particles coated with different protein shells and analyze protein migration.** Prepare separate stock solutions at final concentrations of 0.5 mg/mL protein (GFP or BFP) and 5 mg/mL silica suspension. After 5 min of vortex-mixing, centrifuge to remove the supernatant and resuspend the pellet in 10  $\mu\text{L}$  protein buffer. Combine equal volumes of the two suspensions and image immediately or after 12 h. Migration efficiency is quantified using Mander's overlap coefficients (MOC). The coefficients for GFP and BFP are denoted as  $M_G$  and  $M_B$ , respectively, and are defined as follows:

$$M_G = \frac{\sum(\text{Green, colocal})}{\sum(\text{Green, All})}; M_B = \frac{\sum(\text{Blue, colocal})}{\sum(\text{Blue, All})}$$

**Comparison of LLPS versus MSE fluorescence intensities** For the liquid-liquid phase separation (LLPS) and MSE groups, GFP was adjusted to a final concentration of 30  $\mu\text{M}$ ; the LLPS group was supplemented with 10 % (w/v) PEG 8000, whereas the MSE group received 10 mg/mL silica particles. Both groups were imaged under identical acquisition conditions.

#### Radial Intensity Profile Analysis

Radial fluorescence intensity distributions around mineral particles were extracted from raw image stacks. Distances were binned in one-pixel increments (1  $\mu\text{m}$  per bin in this dataset). For each particle, the mean intensity was computed as a function of radial distance  $r$  (0–100  $\mu\text{m}$ ).

To quantify near- and far-field enrichment, profiles were fitted to a bi-exponential decay model,

$$I(r) = A \cdot \exp(-\lambda_1 \cdot r) + B \cdot \exp(-\lambda_2 \cdot r) + bg$$

where A,B are amplitude coefficients,  $\lambda_1 > \lambda_2 > 0$  are the decay constants for the near- and far-field components, and bg is a constant background. Non-linear least squares fitting was performed in MATLAB (lsqcurvefit, R2023a) using bound-constrained optimization. Initial guesses were set to  $A=0.8 \cdot I_{\max}$ ,  $B=0.2 \cdot I_{\max}$ ,  $\lambda_1=20/L$ ,  $\lambda_2=5/L$  (with L the profile length scale), and bg the minimum observed intensity. Parameters were restricted to non-negative values and the inequality  $\lambda_1 > \lambda_2$  was enforced to ensure physical interpretation.

Goodness of fit was evaluated by the coefficient of determination ( $R^2$ ), root-mean-square error (RMSE), and inspection of residual distributions. Approximate 95% confidence intervals were estimated from the Jacobian of the fit, and parameter correlations were reported from the covariance matrix. For all profiles analyzed, the bi-exponential model outperformed single-exponential alternatives (Akaike information criterion), with representative data shown in Fig. 2b ( $R^2=0.976$ ).

All plots were generated with custom MATLAB routines, displaying experimental data, overall bi-exponential fit, individual near- and far-field components, and residuals (see Fig. 2b).

To ensure physical interpretability, we performed a post-hoc label reordering on the fitted parameters: the numerically larger decay constant  $\lambda$  was reassigned to  $\lambda_1$  (near-field, short-range component) and the smaller to  $\lambda_2$  (far-field, long-range component). Because lsqcurvefit does not admit inequality constraints among parameters, we did not enforce  $\lambda_1 > \lambda_2$  during optimization. Instead, whenever the raw fit returned  $\lambda_1 < \lambda_2$ , we swapped  $A \leftrightarrow B$  and  $\lambda_1 \leftrightarrow \lambda_2$  in post-processing, aligning the output with the manuscript's consistent physical labeling. This relabeling leaves the underlying fit unchanged; it merely standardizes the correspondence between numerical values and their physical meaning.

**Fluorescence Recovery After Photobleaching (FRAP)** was performed on a laser scanning confocal microscope (Olympus FV4000, system version 3.2.1.85) with a 100× oil immersion objective (UPLAPO100XOHR, NA=1.5). The final concentration of GFP and SiO<sub>2</sub> are 0.6 mg/ml and 10 mg/ml respectively. A circular region of interest (ROI) was photobleached using a 488nm laser at 100% power (laser transmissivity setting: 0.5%) with 20 iterations. Time-series acquisition was conducted at 1.4% laser power (488nm) with 21.2s intervals for 7.4 minutes.

#### **Coupling of Enzyme Cascade Reactions on the Surface of the Same Silica (SiO<sub>2</sub>) Particle**

As shown in Figure 3, GOx (final concentration :1 KU/ml, Beyotime), HRP (final concentration:0.2 mg/ml, Beyotime), two kinds of fluorescent proteins (final concentration : of 0.2 mg/ml) were separately added into a centrifuge tube. The mixture was centrifuged at 100 g for 10 seconds. Then, the supernatant was aspirated, and it was washed with 10  $\mu$ l of DI water (Solarbio), followed by brief shaking to mix evenly. Then DI water was replaced by 10  $\mu$ l of substrates solution (glucose with final concentration :1.8 mM, YuanYe, and Amplex Red with final concentration : 0.2  $\mu$ M, YuanYe) . Pictures were shot after 20min of mixing.

#### **Mineral-Surface Templated Compartmentalization through Lipid-Protein Hierarchical Assembly**

The lipid used in the experiments related to Figure 4 is palmitoleic acid (YuanYe), and the fluorescent dye for the lipid is Nile red [In Figures 4b-j, the amount of Nile red added is 1  $\mu$ l (with a concentration of 250  $\mu$ g/ml) for each case. YuanYe]. In Figures 4a and 4b, 1  $\mu$ l of palmitoleic acid was added to 10  $\mu$ l of the silica suspension (with a concentration of 20 mg/ml). In Figures 4d-f, prepare 10  $\mu$ l of silica particles (with a concentration of 20 mg/ml) coated with GFP (with a concentration of 0.4 mg/ml) according to the procedure in Figure 3b. Then, add 2  $\mu$ l of palmitoleic acid and gently shake to mix evenly. In Figures 4g-j, prepare

lipid-coated silica particles with protein films (GFP or BFP) in the same manner as in Figures 4d-f (using proteins and silica particles of the same concentration, and the amount of lipid used is 1  $\mu$ L for each case), and then mix the two together. In Figures 4k-m, prepare lipid-coated silica particles with protein films (GFP + GOx or BFP + HRP, with the concentrations of the fluorescent proteins and enzymes being the same as those in Figure 3) respectively in the same manner as in Figures 4d-f. Then, mix the two together and add the substrate solution (with different substrate concentrations the same as those in Figure 3) to prepare a 10  $\mu$ L suspension. Take photos after 40 minutes of mixing.

**Introducing RT-PCR into a system containing silica dioxide** Suspend the silica particles with 2X q-RT PCR buffer. Then, following the instructions of the kit (Beyotime), add the different components to the suspension, with the total reaction volume being 20  $\mu$ L. The concentration of the template RNA is 140 ng/ $\mu$ L. The sequences of the primers are as follows: 5'-AGAGCTGTTCAGTGGTGTCG & 5'-TAGTTGCGTCACCTTCACCC (For CDS of GFP, synthesized by Sangon Biotech).

**Three-dimensional reconstruction of GFP[SiO<sub>2</sub>] and PAL-GFP[SiO<sub>2</sub>] complexes** The prepared samples were imaged with an inverted fluorescence microscope (Nikon Ti2-E, Japan) equipped with a spinning-disk confocal laser-scanner unit (Nova-SD, Airy Technologies Co., Ltd., China) and a 100 $\times$ /1.49NA objective (Nikon, Japan). For GFP[SiO<sub>2</sub>] complex, GFP and SiO<sub>2</sub> at final concentrations of 0.6 mg/mL and 5 mg/mL. For PAL- GFP[SiO<sub>2</sub>] complex, supplement the above mixture with 0.5  $\mu$ L Rhodamine B dye (10mM in DMSO) and 0.5  $\mu$ L palmitoleic acid.

**Silica-BFP particles  $\pm$  Cy5-PAL: permeation assay of Streptavidin-FITC** Prepare 20  $\mu$ L suspensions of BFP and SiO<sub>2</sub> at final concentrations of 0.5 mg/mL and 5 mg/mL. After 5 min incubation, centrifuge and discard the supernatant. Resuspend the pellets in 10  $\mu$ L protein buffer, add 0.1  $\mu$ L palmitoleic acid containing 10% Cy5-labeled analogue, mix thoroughly, incubate for 5 min, then centrifuge again and remove the supernatant. Finally, resuspend the pellets in 5  $\mu$ L Streptavidin-FITC solution (Beyotime) and incubate for 30 min.

**Analysis of Fluorescence Intensity** All the raw data were obtained using Fiji (Fiji Is Just ImageJ), and the data visualization was carried out with MATLAB R2023b.

**Figure generation** All figures were created with MedPeer (medpeer.cn).

### Author Contributions

**G.Z.Y.:** Conceptualization (supporting), Modeling (equal). Supervision (lead), Validation (lead), Project Administration (lead).

**W.F.C.:** Conceptualization (lead), Methodology (lead), Investigation (lead), Data Analysis and Illustration (lead), Modeling (equal).

**R.F.Z.:** Investigation (supporting), Modeling (equal), Methodology (supporting).

**Z.S.L.:** Investigation (supporting).

**G.Q.W., J.Y.L., H.C.G., H.L., Z.L.W.:** Assistance in investigation.

### Acknowledgements

We express our gratitude to Airy Technologies Co., Ltd., China, for the fluorescence imaging conducted with their spinning-disk confocal microscope (Nova-SD). We express our gratitude to engineer XinYuan Chen of Airy-tech Company for the LSCM operation depicted in Figure



4. We express our gratitude to Hao Xiong, ShiYuan Pei, and Yang Wen for their preparation and reservation of instruments and reagents.

# Supplementary information

## Content

NOTE S1 Theoretical modeling of mineral surface-mediated enrichment.

NOTE S2 Stochastic kinetic simulation of an enzyme-catalyzed cascade reaction.

Supplementary Figure 1 | Adsorption behavior of proteins onto inorganic nanoparticles under elevated-temperature conditions.

Supplementary Figure 2 | Encapsulation of protein-coated silica particles by bubble mediation.

Supplementary Figure 3 | Three-dimensional distribution of the concentration gradient as a function of the diffusion coefficient  $D$  and the radial distance  $r$ .

Supplementary Figure 4 | The reaction dynamics of MSE.

Supplementary Figure 5 | Protein coronas interact with diverse phospholipids and stabilize lipid-mineral suspensions.

## Supplementary Note S1 | Theoretical framework for mineral-surface-mediated enrichment

### S1.1 Physical assumptions

We model protein enrichment around a spherical silica particle of radius  $R$ . The radial distance  $x$  is measured outward from the surface. Two populations coexist: a strongly adsorbed dense layer and a weakly interacting diffuse corona. Within the linear detection range of the microscope, the measured fluorescence intensity  $I(x)$  is proportional to the local concentration  $c(x)$  after subtraction of a constant background. Because the corona thickness  $L$  satisfies  $L \ll R$ , the concentration profile can be treated locally as one-dimensional planar.

### S1.2 Governing equations and boundary conditions

In the diffuse layer, the steady-state concentration satisfies

$$D \frac{d^2 c}{dx^2} - \kappa c = 0 \quad (x > 0)$$

where  $D$  is the effective diffusivity and  $\kappa$  summarizes weak reversible interactions and bulk exchange. At the mineral surface, molecular flux couples to Langmuir exchange with the dense layer:

$$-D \left( \frac{dc}{dx} \right) \Big|_{x=0} = k_{on} c(0) (1 - \theta^*) - k_{off} \theta^*$$

with  $\theta^*$  the surface coverage at quasi-equilibrium. Far from the surface,  $c(x \rightarrow \infty) = c_\infty$ . In

spherical geometry the exact solution is  $c(r) = c_\infty + \frac{A \exp(-\frac{r}{\ell})}{r}$ , which reduces to a planar

exponential  $c(x) = c_\infty + A \exp(-\frac{x}{\ell})$  when  $x \ll R$ .

### S1.3 Bi-exponential representation

Two kinetically distinct modes (strong vs. weak binding) give rise to two characteristic decay lengths  $\ell_1, \ell_2$ . The concentration field is approximated by

$$c(x) = c_\infty + a_1 \exp\left(-\frac{x}{\ell_1}\right) + a_2 \exp\left(-\frac{x}{\ell_2}\right)$$

Thus the measured intensity profile takes the form

$$I(x) = \alpha \exp(-\lambda_1 x) + \beta \exp(-\lambda_2 x) + bg$$

with  $\lambda_i = \frac{1}{\ell_i}$ ,  $\alpha, \beta \geq 0$ , and ordering constraint  $\lambda_1 > \lambda_2$ . We interpret  $(\alpha, \lambda_1)$  as the near-field dense layer and  $(\beta, \lambda_2)$  as the far-field corona.

### S1.4 Parameter estimation

Profiles were fitted by bound-constrained non-linear least squares (MATLAB, lsqcurvefit). Parameters were initialized as described in Methods, with constraints  $\alpha, \beta, bg \geq 0$  and  $\lambda_1 > \lambda_2 > 0$ . Approximate 95% confidence intervals and parameter correlations were computed from the Jacobian. Goodness of fit was evaluated by  $R^2$ , RMSE, residual inspection, and comparison with single- and three-exponential models using the Akaike information criterion. Note: To facilitate physical interpretation and maintain consistency with the graphical conventions employed herein, we adopt the “decay-constant magnitude” labeling convention:  $\lambda_1$  denotes the numerically larger decay constant (corresponding to the shorter length scale  $\ell_1 = 1/\lambda_1$ , i.e., the near-field dense layer), whereas  $\lambda_2$  denotes the smaller decay constant (corresponding to the longer length scale  $\ell_2 = 1/\lambda_2$ , i.e., the far-field loose corona).

Whenever the raw fitting output yields the opposite order, we swap the parameters in the reported results to adhere to this definition (see Methods).

### **S1.5 Phase Separation Dynamics**

We postulate that, under certain specific circumstances—such as transient fluctuations in local concentration—the surface-adsorbed concentration of biomacromolecules on inorganic particles can exceed the threshold required for LLPS in the bulk phase, giving rise to Supplementary Fig. 3.

The critical condition for liquid-liquid phase separation (LLPS) nucleation:

$$c(\mathbf{r}) - c_{crit} > 0$$

Integrating the derived analytical expression with the data presented in Supplementary Fig. 3, we conclude that (i) nucleation of phase separation is increasingly favored in regions proximal to the inorganic particle surface, and (ii) molecules possessing a larger diffusion coefficient  $D$  exhibit a higher propensity for such nucleation.

## **NOTE S2**

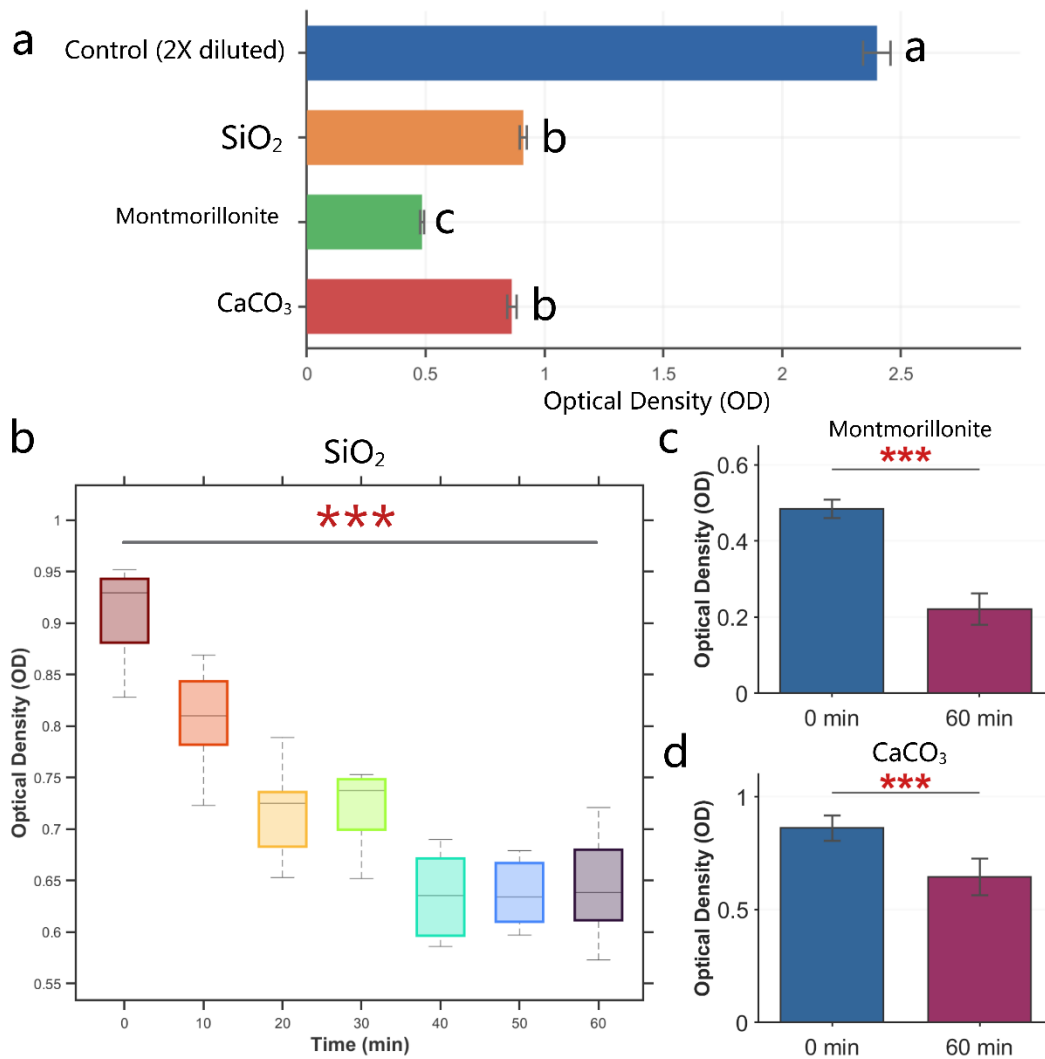
### **Stochastic kinetic simulation of an enzyme-catalyzed cascade reaction.**

#### **Basic Assumptions**

We presume that the space is a cube. The reaction process entails the substrate being catalyzed by enzyme I to yield an intermediate product, which is subsequently catalyzed by enzyme II to produce the final product (Fig. 3). The substrate, intermediate product, and final product can diffuse freely, while the enzymes remain fixed in their original locations. At each time interval, the substrate, intermediate product, and final product experience stochastic diffusion. The reaction probability is ascertained from the catalytic constants of the enzymes and the time interval.

By integrating prior research with our findings, we have modeled the cascade reactions under two specific conditions: 1. the bulk dilute condition (Bulk), and 2. the MSE condition. In the bulk condition, the enzymes are uniformly dispersed throughout the entire volume; in the MSE condition, the enzymes are randomly distributed within a spherical corona region. The substrate molecules are initially dispersed randomly throughout the entire space, excluding the interiors of inorganic particles.

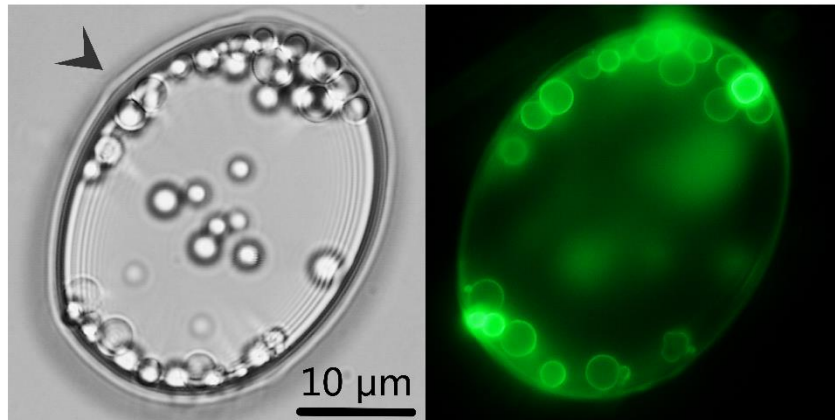
To quantitatively assess the kinetic properties of mineral surface-mediated enrichment, we conducted stochastic simulations of a two-step enzymatic cascade fixed on a center particle. The model exhibits a surge in catalytic activity, characterized by elevated beginning reaction rates that swiftly deplete the localized substrate reservoir (Supplementary Fig. 4a-b). Significantly, our simulations demonstrate the spontaneous development of a pronounced substrate concentration gradient, with reactants markedly concentrated toward the enzyme-coated surface (Supplementary Fig. d-e). This localized molecule crowding markedly increases catalytic throughput, establishing a microenvironment that serves as an analogy to primitive substrate channeling and successfully mitigates the diffusion constraints of a dilute bulk solution. The computational results robustly substantiate our hypothesis that mineral interfaces can function as foundational scaffolds for the organization of proto-metabolic pathways, thereby creating the localized, non-equilibrium conditions essential for the emergence of complex systems chemistry on early Earth.



**Supplementary Figure 1 | Adsorption behavior of proteins onto inorganic nanoparticles under elevated-temperature conditions.**

(a) The optical density (OD) of supernatants was measured following a 60-minute incubation at 70°C. Control: BSA solution (2× diluted with buffer); experimental groups: 10 mg/mL  $\text{SiO}_2$ , montmorillonite, or  $\text{CaCO}_3$  combined with 1 mg/mL BSA. Temporal OD profiles for  $\text{SiO}_2$  (b), montmorillonite (c), and  $\text{CaCO}_3$  (d) systems. Reduced heating durations (<60 min) were offset by incubation at ambient temperature. Error bars:  $\pm$ s.d. (n=8); letters and \*\*\* denote significant inter-group differences with  $P < 0.001$  (compared to 0-min control), respectively.

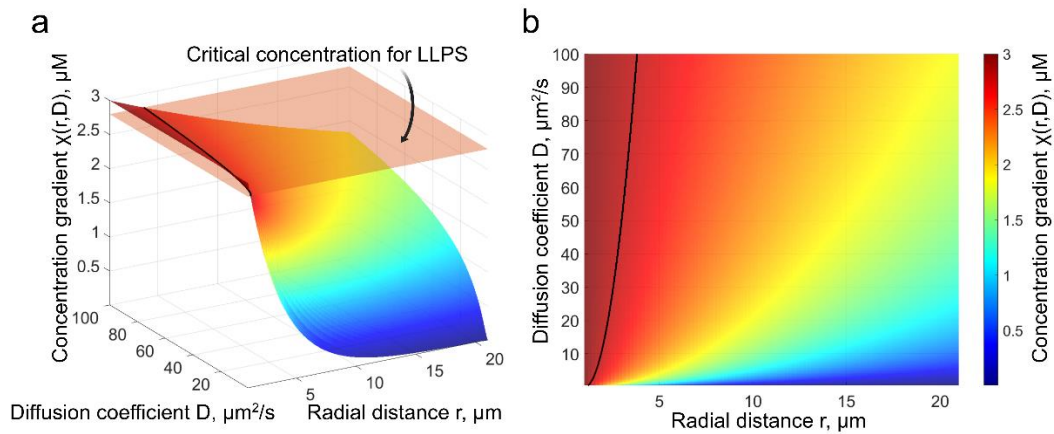
a



Supplementary Figure 2 | Encapsulation of protein-coated silica particles by bubble mediation.

(a) (Left) Bright-field micrograph depicting a gas bubble (arrowhead) with many silica particles. (Right) Fluorescence micrograph validating protein localization (green) on silica particles within the bubble structure. Scale bar, 10  $\mu\text{m}$  (applicable to both panels).

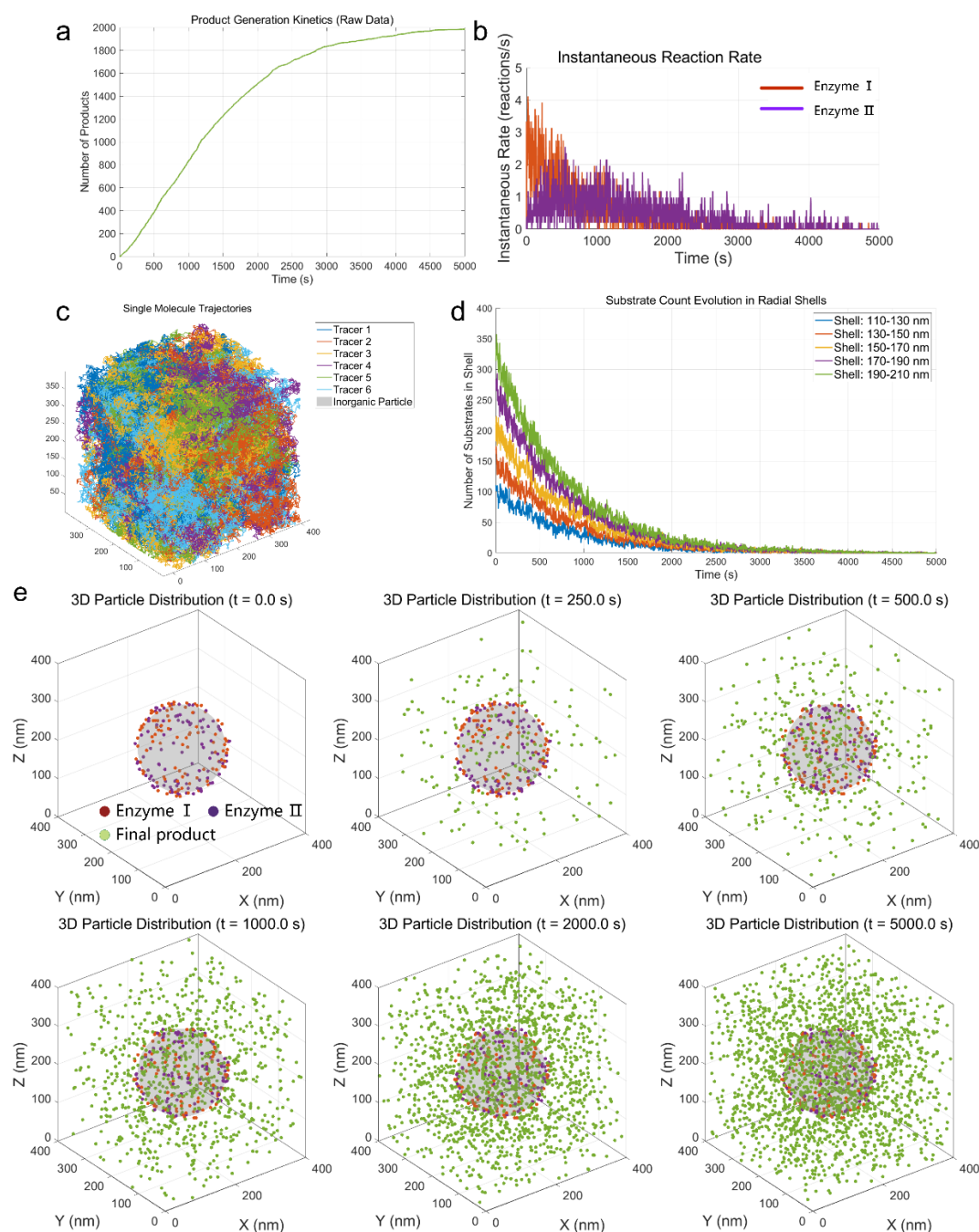




**Supplementary Figure 3 | Three-dimensional distribution of the concentration gradient as a function of the diffusion coefficient  $D$  and the radial distance  $r$**

(a) When, under certain conditions, the local concentration of macromolecules on an inorganic surface exceeds the phase-separation threshold (surface lying above the pink plane), liquid–liquid phase separation may nucleate at these loci.

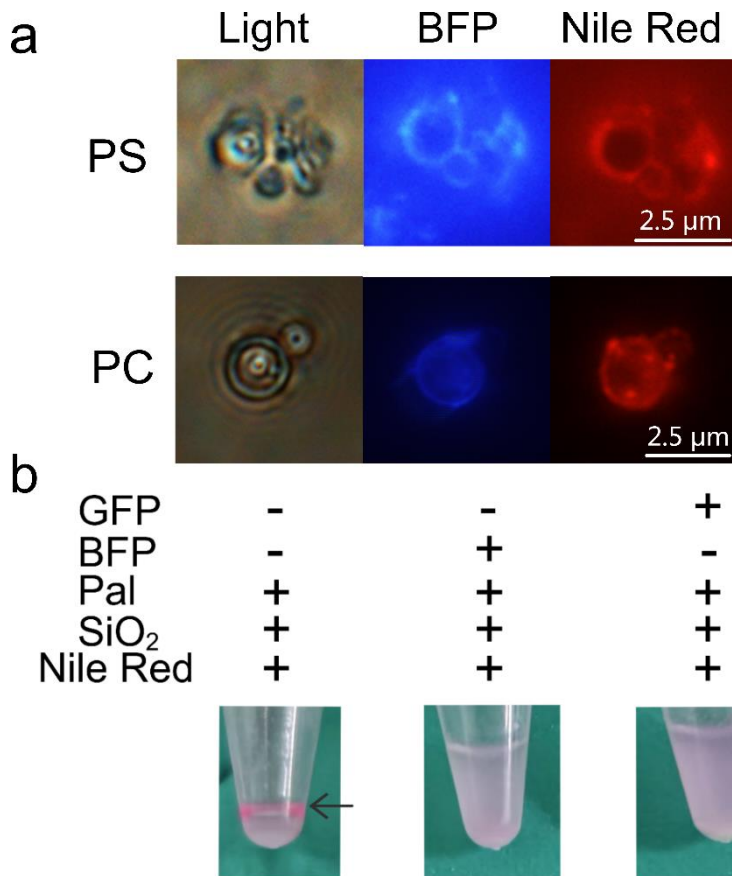
(b) Top-down view: regions to the left of the solid black line denote sites where LLPS nucleation is permissible.



**Supplementary Figure 4 | The reaction dynamics of MSE**

(a) Cumulative product development curve. The parameters of the simulation code are delineated as follows: The reactive cubic domain possesses an edge length of 500 nm, with a total simulation duration of  $T = 5000.0$  s and a time step of  $dt = 0.1$  s. The inorganic particle has a diameter of 100 nm. The quantities of the two enzymes are each 100, exhibiting catalytic efficiencies ( $K_{cat}$ ) of 100 1/s. At  $t = 0$ , the substrate count is 2000. The diffusion coefficient for small molecules (substrates, intermediates, and final products) is established at  $100 \text{ nm}^2/\text{s}$ ; the enzyme film thickness is 10 nm, with enzymes randomly distributed within this film; we assume the diameters of the enzymes are 2 nm, while the diameters of the small molecules are 1 nm. (b) Instantaneous reaction rates of two enzymes, we define it as reactions per second. (c) Independently monitor the

motions of six small molecules. Any molecule that undergoes conversion—be it from substrate to intermediate or from intermediate to end product—remains classified as a singular small molecule. (d) Quantify the quantity of substrate molecules within uniform shells of 20nm thickness surrounding the surface of the inorganic particle. (e) Snapshots of the reaction progress at successive time points.



Supplementary Figure 5 | Protein coronas interact with diverse phospholipids and stabilize lipid-mineral suspensions.

(a) Co-localization of phosphatidylserine (PS) and phosphatidylcholine (PC) with the protein corona on silica particle surfaces. From left to right: bright-field, BFP, and Nile Red channels. Scale bars: 2.5  $\mu\text{m}$ .

(b) This picture illustrates the states of samples comprising palmitoleic acid (Pal), silica (SiO<sub>2</sub>), Nile red (Nile), coupled with the incorporation of BFP and GFP, respectively, following mixing. The left-hand centrifuge tube, containing solely Pal, SiO<sub>2</sub>, and Nile, displays clear stratification (as indicated by the arrow). Conversely, the middle and right-hand centrifuge tubes, upon the incorporation of BFP and GFP respectively, yield suspensions. The three sets of centrifuge tubes depicted in this picture include silica particles at a concentration of 20 mg/ml, palmitoleic acid comprising 1/12 of the total volume, a Nile red solution at 250  $\mu\text{g/ml}$  also constituting 1/12 of the total volume, and protein at a concentration of 0.5 mg/ml. Microscopic analysis reveals that the presence of protein modifies the interaction between free lipids and minerals.

FUS-IDR-sfGFP	EBFP-hnRNPA1-IDR
MASNDYTQQATQSYGAYPTQPGQGYSSQSSQPY GQSYSGYGQSADTSYGQSSYGSSYGQTQNTG YGTQSAPQGYGSTGGYGSSQSSYGQSSYPG YGQQPAPSSTSGSYGGSSQSSYGQPQSGGYGQQ SGYGGQQQSYGQQQSSYNPPQGYGQQNQYNSS SGGGGGGGGNYGQDQSSMSGGGGGGGYGNQ DQSGGGGGGYGGGQQDRGMSKGEELFTGVVPIL VELDGDVNGHKFSVRGEGEGDATNGKLTGKFICTT GKLPVPWPPTLVTTLTYGVCFSRYPDHMKRHDFK SAMPEGYVQERTISFKDDGTYKTRAEVKFEGDTLVN RIELKGIDFKEDGNILGHKLEYNFNHNVYITADKQK NGIKANFKIRHNVEDGSVQLADHYQQNTPIGDGP VLLPDNHVLTQSVLSKDPNEKRDHMLLEFVTAA GITHGMDELYK	MVSKEELFTGVVPILVELDGDVNGHKFSVRGEGE GDATNGKLTGKFICTTGKLPVPWPPTLVTTLSHGVQC FARYPDHMKQHDFKFSAMPEGYVQERTIFFKDDGT YKTRAEVKFEGDTLVNRIELKGVDKEDGNILGHKLE YNFNHNVYITADKQKNGIKVNFKIRHNVEDGSVQ LADHYQQNTPIGDGPVLLPDSHYLTQSVLSKDPN EKRDHMLLEFRTAAGITLGMDELYKMASASSSQR GRSGSGNFGGGRGGGFGGNDNFGRGGNFSGRGG FGGSRGGGGYGGSGDGYNGFGNDGSNFGGGGSY NDFGNYNQSSNFGPMKGGNFGGRSSGPYGGG GQYFAKPRNQGGYGGSSSSSYGSGRRF

**Table S1 | the sequences of two fluorescent proteins**

The sequences of the two fusion proteins were engineered into the pET - 28a(+) plasmid and expressed in the BL21(DE3) strain. This construction strategy was deliberately designed to ensure that the resultant fused proteins harbored a 6×His tag. The cloning sites selected for this manipulation were **Nde I** and **Xho I**. The sequence synthesis and plasmid construction were served by Sangon Biotech Company.

**Table S2 | The composition of non - denaturing lysis/washing/elution/dialysis buffer (pH=8.0).**

Reagents	Final concentration	Source
NaH <sub>2</sub> PO <sub>4</sub>	50mM	Beyotime
NaCl	300mM	Beyotime
ddH <sub>2</sub> O	n/a	Solarbio

Reagents	Final concentration	Source
NaH <sub>2</sub> PO <sub>4</sub>	50mM	Beyotime
NaCl	300mM	Beyotime
imidazole	2mM	Beyotime
ddH <sub>2</sub> O	n/a	Solarbio

Reagents	Final concentration	Source
NaH <sub>2</sub> PO <sub>4</sub>	50mM	Beyotime
NaCl	300mM	Beyotime
imidazole	50mM	Beyotime
ddH <sub>2</sub> O	n/a	Solarbio

Reagents	Final concentration	Source
1M Tris-HCl, pH=7.4	50mM	Beyotime
NaCl	25mM	Beyotime
Glycerol	10%	YuanYe
ddH <sub>2</sub> O	n/a	Solarbio

## Reference

1. Ianeselli A, Tetiker D, Stein J, Kühnlein A, Mast CB, Braun D, *et al.* Non-equilibrium conditions inside rock pores drive fission, maintenance and selection of coacervate protocells. *Nature Chemistry* 2022, **14**(1): 32-39.
2. Hansma HG. The power of crowding for the origins of life. *Orig Life Evol Biosph* 2014, **44**(4): 307-311.
3. Akbari A, Palsson BO. Metabolic homeostasis and growth in abiotic cells. *Proc Natl Acad Sci U S A* 2023, **120**(19): e2300687120.
4. Cleaves HJ. Prebiotic Chemistry: What We Know, What We Don't. *Evolution: Education and Outreach* 2012, **5**(3): 342-360.
5. de Herrera AG, Markert T, Trixler F. Temporal nanofluid environments induce prebiotic condensation in water. *Communications Chemistry* 2023, **6**(1): 69.
6. Akbari A, Palsson BO. Positively charged mineral surfaces promoted the accumulation of organic intermediates at the origin of metabolism. *PLoS Comput Biol* 2022, **18**(8): e1010377.
7. Zaia DA. A review of adsorption of amino acids on minerals: was it important for origin of life? *Amino Acids* 2004, **27**(1): 113-118.
8. Han Q, Candiloro ZPJ, Cai X, El Mohamad M, Dyett BP, Rosado CJ, *et al.* Silica Nanoparticle-Protein Aggregation and Protein Corona Formation Investigated with Scattering Techniques. *ACS Appl Mater Interfaces* 2025, **17**(5): 8574-8587.
9. Shi B, Shin YK, Hassanali AA, Singer SJ. DNA Binding to the Silica Surface. *J Phys Chem B* 2015, **119**(34): 11030-11040.
10. Erastova V, Degiacomi MT, D GF, Greenwell HC. Mineral surface chemistry control for origin of prebiotic peptides. *Nat Commun* 2017, **8**(1): 2033.
11. Holler S, Bartlett S, Löffler RJG, Casiraghi F, Diaz CIS, Cartwright JHE, *et al.* Hybrid organic-inorganic structures trigger the formation of primitive cell-like compartments. *Proc Natl Acad Sci U S A* 2023, **120**(33): e2300491120.
12. Sojo V, Herschy B, Whicher A, Camprubí E, Lane N. The Origin of Life in Alkaline Hydrothermal Vents. *Astrobiology* 2016, **16**(2): 181-197.
13. Chen J, Bai Q, Li Y, Liu Z, Li Y, Liang D. Coacervates Forming Coexisting Phases on a Mineral Surface. *Langmuir* 2023, **39**(16): 5814-5824.



14. Haugerud IS, Jaiswal P, Weber CA. Nonequilibrium Wet-Dry Cycling Acts as a Catalyst for Chemical Reactions. *J Phys Chem B* 2024, **128**(7): 1724-1736.
15. Nogal N, Sanz-Sánchez M, Vela-Gallego S, Ruiz-Mirazo K, de la Escosura A. The protometabolic nature of prebiotic chemistry. *Chem Soc Rev* 2023, **52**(21): 7359-7388.
16. Parsons I, Lee MR, Smith JV. Biochemical evolution II: origin of life in tubular microstructures on weathered feldspar surfaces. *Proc Natl Acad Sci U S A* 1998, **95**(26): 15173-15176.
17. Klein G, Mathé C, Biola-Clier M, Devineau S, Drouineau E, Hatem E, *et al.* RNA-binding proteins are a major target of silica nanoparticles in cell extracts. *Nanotoxicology* 2016, **10**(10): 1555-1564.
18. Xie M, Hansen AL, Yuan J, Brüscheweiler R. Residue-Specific Interactions of an Intrinsically Disordered Protein with Silica Nanoparticles and their Quantitative Prediction. *J Phys Chem C Nanomater Interfaces* 2016, **120**(42): 24463-24468.
19. Mathé C, Devineau S, Aude JC, Lagniel G, Chédin S, Legros V, *et al.* Structural determinants for protein adsorption/non-adsorption to silica surface. *PLoS One* 2013, **8**(11): e81346.
20. Ma Q, Wang J, Yu H, Sun J, Sun J, Chen J, *et al.* Protocol to alter a protein's phase separation capacity to control cell fate transitions. *STAR Protoc* 2021, **2**(4): 100887.
21. Martin EW, Thomasen FE, Milkovic NM, Cuneo MJ, Grace CR, Nourse A, *et al.* Interplay of folded domains and the disordered low-complexity domain in mediating hnRNPA1 phase separation. *Nucleic Acids Res* 2021, **49**(5): 2931-2945.
22. Martin EW, Harmon TS, Hopkins JB, Chakravarthy S, Incicco JJ, Schuck P, *et al.* A multi-step nucleation process determines the kinetics of prion-like domain phase separation. *Nat Commun* 2021, **12**(1): 4513.
23. Ji Y, Lin Y, Qiao Y. Plant Cell-Inspired Membranization of Coacervate Protocells with a Structured Polysaccharide Layer. *J Am Chem Soc* 2023, **145**(23): 12576-12585.
24. Agrawal A, Radakovic A, Vonteddu A, Rizvi S, Huynh VN, Douglas JF, *et al.* Did the exposure of coacervate droplets to rain make them the first stable protocells? *Sci Adv* 2024, **10**(34): eadn9657.
25. Castellana M, Wilson MZ, Xu Y, Joshi P, Cristea IM, Rabinowitz JD, *et al.* Enzyme clustering accelerates processing of intermediates through metabolic channeling. *Nat Biotechnol* 2014, **32**(10): 1011-1018.

26. Dai S, Xie Z, Wang B, Ye R, Ou X, Wang C, *et al.* An inorganic mineral-based protocell with prebiotic radiation fitness. *Nature Communications* 2023, **14**(1): 7699.
27. Hazen RM, Sverjensky DA. Mineral surfaces, geochemical complexities, and the origins of life. *Cold Spring Harb Perspect Biol* 2010, **2**(5): a002162.
28. Guo W, Kinghorn AB, Zhang Y, Li Q, Poonam AD, Tanner JA, *et al.* Non-associative phase separation in an evaporating droplet as a model for prebiotic compartmentalization. *Nat Commun* 2021, **12**(1): 3194.
29. Guo D, Zhang Z, Sun J, Zhao H, Hou W, Du N. A Fusion-Growth Protocell Model Based on Vesicle Interactions with Pyrite Particles. *Molecules* 2024, **29**(11).
30. Maurer S. The Impact of Salts on Single Chain Amphiphile Membranes and Implications for the Location of the Origin of Life. *Life (Basel)* 2017, **7**(4).
31. Wołos A, Roszak R, Źądło-Dobrowolska A, Beker W, Mikulak-Klucznik B, Spólnik G, *et al.* Synthetic connectivity, emergence, and self-regeneration in the network of prebiotic chemistry. *Science* 2020, **369**(6511).